Proceedings 10th NUMGE 2023
10th European Conference on Numerical Methods in Geotechnical Engineering
Zdravković L, Konte S, Taborda DMG, Tsiampousi A (eds)
ISSN

doi: 10numge-2023-Y-XXXX

Cone Penetration Tests (CPTs) in layered soils: a Material Point approach

R. Bird [1], W.M. Coombs [1], C.E. Augarde [1], M.J. Brown [2], Y. Sharif [2], G. Gareth [3], K. Johnson [3]

[1]*Department of Engineering, Durham University, Durham, England, UK*
[2] *School of Science and Engineering, University of Dundee, Dundee, Scotland, UK*
[3]*British Geological Survey, Edinburgh, Scotland, UK*

ABSTRACT: Cone Penetration Tests (CPTs) can be used to determine *in-situ* soil properties and represent a practical choice for site investigation offshore, especially for linear infrastructure, such as offshore wind export cables. Information gained from CPTs is key for predicting soil-structure interaction behaviour, for example when predicting the tow forces involved in seabed ploughing, as the CPT provides an analogue to the process. The numerical modelling of CPTs is challenging due to the significant distortion in the soil displaced by the penetrating cone. This means that solving this sort of problem using finite elements, although not impossible, is numerically tiresome in terms of remeshing and mapping of state variables. Therefore, in this paper we adopt the Material Point Method (MPM) to develop a CPT prediction tool in layered soils. This MPM is combined with a novel non-matching mesh frictional boundary to represent the penetrometer. The developed tool will be used to understand the response of layered soils commonly found offshore as a step towards predicting the interaction of ploughs and anchors with the seabed.

Keywords: Cone Penetration Tests; Material Point Method; Sand; Layered Soils.

1 INTRODUCTION

Cone penetration tests (CPTs) are used to predict *in-situ* material properties, necessary for engineers designing foundations for wind turbines both on- and offshore (Robinson *et al.*, 2021) . The advantage of CPTs is that they are a relatively simple test to perform, and can map the layering often found in the UK of different density sands and clays, (Mellet *et al.*, 2015). Numerical modelling of a CPT might be required to validate the material parameter values used in a more complex numerical model of a geotechnical problem, however numerical simulation of a CPT is complex since it combines the non-linearities of finite strain theory, elastoplastic material behaviour, contact and friction. The combination of these non-linearities makes the CPT inherently difficult to model requiring traditional numerical schemes, such as finite elements, to be extended to Arbitrary Lagrangian Eulerian (ALE) formulations (Tolooiyan and Gavin, 2011).

The material point method (MPM) is a natural alternative to finite elements for numerical CPT simulations since it is well suited to large deformation problems. The solid mechanics problem is still solved on a background grid (or mesh) of finite elements, however the data for the problem is stored at material points (MPs) which move as a function of the grid deformation (Coombs and Augarde, 2020a). As the solution proceeds, the material points convect through the background grid carrying their material and stress states whilst the grid remains unchanged. For large deformation problems this avoids solving with highly skewed elements, or requiring treatment in the form of remeshing and mapping of variables.

The MPM has been used in recent years for a range of geotechnical problems such as slope stability (Wang *et al.*, 2016), landslide runout (Llano-Serna *et al.*, 2016), and modelling of viscoelastic material in the Earth's mantle (Moresi, 2007). Focussing on modelling of CPTs, Martinelli and Vahi (2021) used the MPM to model both the global force-displacement response in a CPT and provide a numerical framework for characterization of soils where limited data exists. How the CPT cone interacts with the soil, within an MP setting, is an active area of research (Gao *et al*., 2022; Lei *et al*., 2022; Nakamura *et al.*, 2021)because the material domain is represented with points, with an associated volume, and hence the boundary of the soil is undefined; although methods do exist to model the boundary (Bing *et al.*, 2019). Interaction between the rigid cone and the soil is tackled using contact mechanics approaches. Numerous contact methods have recently been proposed for the MPM, for example: MP-to-MP contact where the rigid body is represented as a stiff set of material points and contact occurs at the MP level (Gao *et al.*, 2022), and MP to rigid body contact (Nakamura *et al.*, 2021), where

the MP has a radius, associated with its representative material volume which interacts with a rigid body which does not conform to the background grid. When the interaction occurs, normal and tangential contact forces are then mapped to the background mesh nodes corresponding to the material point. This is similar to MPM contact algorithms presented in the computer graphics research community (Hu *et al.*, 2018), where arbitrary complex shapes in 3D are considered and realistic *looking* results achieved. Another choice is to represent the cone as part of the grid boundary, using an unstructured background grid. However, remeshing is potentially required as the cone moves and, like finite elements, it is possible to create highly skewed elements, (Martinelli and Vahi, 2021).

In this paper a quasi-static implicit MP approach suited for modelling CPTs is presented. The approach involves non-linear penalty enforced contact with a rigid body. The advantage of a quasi-static implicit analysis is that facilitates larger time (or load) increments compared to explicit approaches. This is of particular importance for numerical CPTs due to the requirement of a fine mesh around the cone, and the long simulated time for the slow penetration. It also negates the requirement of damping to reach a steady state solution (and the associated parameter tuning).

2 CONTACT WITH THE MATERIAL POINT METHOD

2.1 Material point method

Initially the MPM was developed from an earlier explicit method for fluids (Sulsky *et al.*, 1994) and was later extended to its implicit form for quasi-static solid mechanics problems by Guilkey and Weiss, (2003). The MPM operates by the MPs carrying all material and state information corresponding to their location and subsequently convecting as the problem evolves. The problem itself is solved incrementally on a background finite element grid by mapping the MP data for the problem to the grid using a finite element basis. Once an increment has been solved the updated state information is stored at the MP, in its new location, and the background mesh is reset to its original configuration. In this work, the Generalised Interpolation Material Point Method (GIMPM) is used, an extension of the MPM, to remove grid crossing errors and to improve convergence with refinement (Charlton *et al.*, 2017).

The system of equations for solving the updated Lagrangian GIMPM are summarised here with matrix [·] and vector {·} notation. This is necessary so that in the next section the interaction of the rigid body with the MPs can be described within the same framework. A fully detailed description, with corresponding open-source code, can be found in Coombs and Augarde, (2020a). The shape function matrix that maps material point data to its corresponding grid nodes is $[S_{vp}]$, where p is the material point number and v is the node (or vertex) of the background grid, and its corresponding derivative is $[\nabla S_{vp}]$. The mapping of body forces that act on the material point $\{b_p\}$ to the grid nodes is expressed as

$$\{F_{ext}\} = \sum_{p\in MP}[S_{vp}]^T \{b_p\}V_p, \qquad (1)$$

where $\{F_{ext}\}$ is the external force vector for all the nodes in the problem, $\sum$ is the usual finite element assembly operator, MP is the set of all material points and V_p is the volume of the material point p. The internal stress is similarly mapped to the nodes using the shape function derivative,

$$\{F_{int}\} = \sum_{p\in MP}[\nabla S_{vp}]^T \{\sigma_p\}V_p \qquad (2)$$

where $\{F_{int}\}$ is the internal force vector and $\{\sigma_p\}$ is the internal Cauchy stress at the MP. With these two equations the residual for the problem can be written as $\{F_R\} = \{F_{int}\} - \{F_{ext}\}$. Here the Newton-Raphson solution scheme is used to solve the non-linear problem,

$$\{\delta u_i\} = -[K_R]^{-1}\{f_{R,i-1}\} \qquad (3)$$

where $\{\delta u\}$ is the incremental nodal vector of displacements of the background grid, i is the iteration step within the load increment. $[K_R]$ is the tangent stiffness matrix, formed by finding the direction derivative of $\{F_R\}$ in the direction $\{\delta u_i\}$ at $\{u_i\}$, and lastly the total displacement over the load increment is $\Delta u = \sum_i \delta u_i$. See Section 6.3 of Coombs *et al.* (2020b) for more details.

2.2 Rigid body description

Now that the framework of the GIMPM has been outlined, the interaction between the rigid body and the MPs can be described.

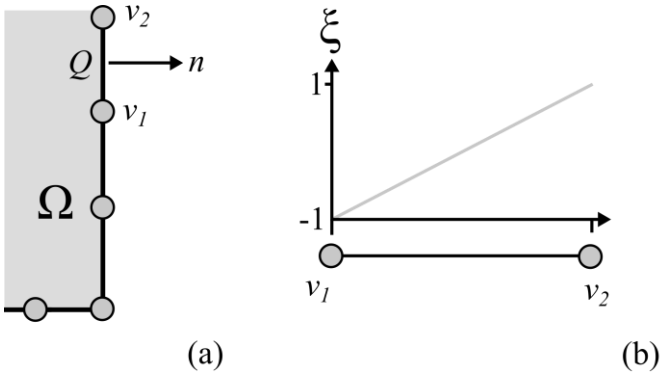

Figure 1. The discretisation of the rigid body domain Ω into Q and its corresponding local coordinate (b).

The current load step is defined as m and the geometry of the rigid body is defined as Ω, see *Figure 1*, with a boundary $\partial\Omega$ that is divided into a contiguous set of line elements $Q \in \partial\Omega$, each with their own normal n_Q, and two vertices $v_j^Q(x)$; $j \in [1,2]$, x is the vertex position in the problem domain and $\xi(v_1^Q, v_2^Q) \in [-1,1]$ is a local coordinate that varies linearly between the two vertices of the element Q.

2.3 *Normal penalty contact*

Due to its numerical simplicity, a non-linear normal penalty method is used to weakly enforce contact between the MP p and the position of the rigid body at the current load step, Ω_m. It is a weak contact condition since an allowable small overlap exists between the MP and rigid body. The normal penalty force f_p is the force normal to Ω_m that acts in the direction n_Q. It is a function of the overlap D of the MP volume with the element Q, where Q is found through a closest point projection (Wriggers, 2006). To improve the convergence of the Newton-Raphson scheme, and to generally improve the contact behaviour of MPs and the rigid body, the penalty force is smoothed, similar to the method proposed by Ma *et al.* (2014). This is achieved by defining a function that makes the contact force variation C^1 between the states of no-contact and contact; this achieved by considering a domain around the MP, as in *Figure 2*.

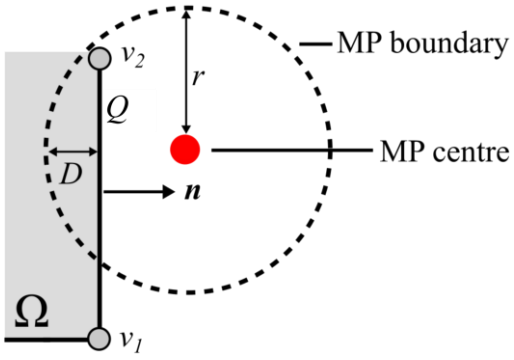

Figure 2. Penetration of the MP with the rigid body domain.

The material has an effective radius $r = \left(V_p^{m-1}\right)^{\frac{1}{2}}$, where V_p^{m-1} is the volume associated with the material point at the end of previous load step. As *Figure 2* shows, the penetration, D, is defined in terms of the overlap of the MP boundary with Q. Compared with using the MP centre, the material associated with the MP overlapping the rigid body
is minimised and with a penetration function can provide a *softer* transition between no contact and contact states. The penetration function is defined as $f_D(D)$, with the variables described in *Figure 2*, where

$$f_D(D) = \begin{cases} \frac{c_D D^2}{r} & \text{if } 0 \le D \le r \\ c_D(2D - r) & D > r \end{cases} \quad (4)$$

where c_D is the penalty constant for normal penetration. This penalty contact force is a point force acting on the background grid element at the MP position, it is therefore projected onto the background grid with

$$\{F_D\} = \sum_{p \in MP} \left[S_{vp}\right]^T \{n\} f_D^p \,, \quad (5)$$

where $\{F_D\}$ is the nodal normal contact force for all nodes in the grid.

2.4 *Coulomb friction with material points*

The stick-slip Coulomb friction law is used here to model the frictional interface between MPs and the rigid body. The total sliding of a point along a body is the summation of the total stick and slip sliding that has occurred

$$g^m = g_l^m + g_t^m \,, \quad (6)$$

where g is a scalar for the slip that has occurred in the tangential direction; set as positive for movement along the rigid body in the anticlockwise direction for 2D simulations. The subscripts l and t correspond to the sliding in the slip and stick modes respectively. For algorithmic simplicity and regularisation of the Coulomb law, a penalty stick-slip formulation is used, whilst noting its violation of the KKT conditions. Considering the analogy for plasticity, the Coulomb friction for stick-slip criteria is presented as a yield surface

$$\lambda = |t_m| - \mu c_D D_m \le 0. \quad (7)$$

Sticking modes exist inside the surface and slipping modes on the surface, and t_m is the frictional traction load for the current load step. To determine the friction state and the traction load, a trial traction is used,

$$t_m^{tr} = -c_t\left(g^m - g_l^{m-1}\right) = t_{m-1} - c_t \Delta g, \quad (8)$$

where $\Delta g = g^m - g^{m-1}$ is the relatively incremental movement of the MP along the rigid body. This is calculated using a closest point projection (CPP) of the converged state of the MP onto $\partial\Omega$ for increment $m-1$, and a CPP of the MP onto $\partial\Omega$ for the current state m. If *Equation (7)* is true for the trial traction, then the point is sticking and $t_m = t_m^{tr}$. Otherwise, the material is slipping, and the trial traction is mapped back onto the sliding yield surface, which for a constant μ is

$$t_m = \mu c_D D_m (t_m^{tr} / |t_m^{tr}|). \quad (9)$$

The benefit of using (8) with the previous traction load, t_{m-1}, and Δg, is that minimal geometric information is stored. Only the previous location of the MP projected onto $\partial\Omega_{m-1}$ is required. Finally, the tangential component of the traction is projected on the background mesh as

$$\{F_T\} = \sum_{p\in MP}\left[S_{vp}\right]^T \{n^{||}\} t_m^p. \quad (10)$$

2.5 Contact tangent stiffness matrices

Since the contact problem is solved implicitly the contact forces, and their respective linearisation with respect to the grid displacements, need to be added to *Equation (3)* so that the problem can be solved using the Newton-Raphson method. The linearisation of the discrete form of the normal force takes the form

$$[K_D] = \sum_{p\in MP}\left[S_{vp}\right]^T \{n\}\{n\}^\top\left[S_{vp}\right] \quad \left(\frac{\partial f_D}{\partial D}\right). \quad (11)$$

For the tangential force, *Equation (8)*, the linearisation for stick is

$$[K_T] = -\sum_{p\in MP} c_N\left[S_{vp}\right]^T \{n^{||}\}\{n^{||}\}^\top\left[S_{vp}\right] \quad (12)$$

and slip, from *Equation (9)*, is

$$[K_T] = -\sum_{p\in MP}\left[S_{vp}\right]^T \{n^{||}\}\{n\}^\top\left[S_{vp}\right]\mu c_n\left(\frac{\partial f_D}{\partial D}\right). \quad (13)$$

Including *Equations (11), (12) and (13)* into *Equation (3)* gives the complete system of linearised equations to be solved,

$$\{\delta u_i\} = -[K]^{-1}\{f_R + F_D + F_T\}, \quad (14)$$

where $[K]$ is the summation of the stiffness components from the MPs and the boundary interaction terms.

3 NUMERICAL CPT

Two experiments are shown here, first a validation to demonstrate that the friction contact model produces accurate results with experimental data, followed by an analysis of a CPT in a layered sand sample.

3.1 Validation setup

To validate the implementation the results are compared to the CPT data obtained by Davidson *et al.* (2022) in which the CPT was performed in a centrifuge where the top of sample experienced $40g$ whilst the bottom of the sample experienced $50g$. A centrifuge increases the "gravitational" load the test sample experiences and hence increases the stress that would otherwise be experienced from gravitational load, thus a greater effective depth, larger than the true depth, can be experimented upon. The effective depth is determined for this experiment

$$h = \left(\frac{10}{0.4}\right) z^2 + 40z \quad (15)$$

where z is the penetration depth into the experimental sample. The geometry of the material sample and the CPT, for both the experiment and its corresponding scaling are provided in Table 1.

Table 1. Geometry data for the material sample and CPT.

Dimension	Experiment	Scaled
Sample depth	434 mm	20 m
Sample radius	200 mm	12.5 m
Penetration depth	200 mm	10 m
Cone radius	8 mm	0.4 m

The model domain and boundary conditions are shown in *Figure 3a* with the corresponding representation of the mesh in *Figure 3b*. *Figure 3a* shows a 2D axisymmetric domain, with the left most edge of the domain as the axis of rotational symmetry. On the bottom and exterior edge roller boundary conditions are enforced and the Ghost Penalty method (Coombs, 2022) is used to stabilise the system of equations. The iGIMP formulation is used (Charlton *et al.*, 2017), with the corner point update of the GIMP domains to avoid very high aspect ratios of the representative volumes (Coombs *et al.*, 2020b).

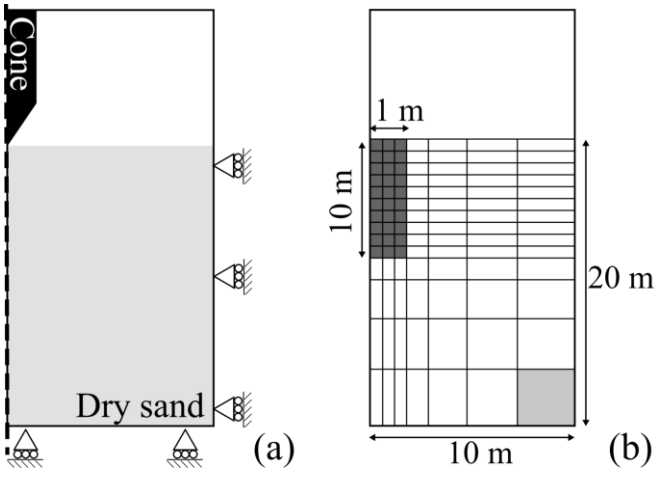

Figure 3. Validation: (a) shows the boundary conditions to the domain with a not-to-scale background mesh shown in (b).

For clarity a not-to-scale mesh sketch is shown in *Figure 3b*. The elements shaded in dark grey are square with side length 0.1m, all elements were initialised with 4 (2-by-2) MPs. The mesh was created using a power law to

the size of the square light grey element, in the bottom right, with side length 3.25 m.

A linear elastic-perfectly plastic constitutive model with a Drucker-Prager yield surface is used to represent the sand. The material properties are determined from Brinkgreve *et al.* (2010) for a dry sand with a relative density of 38% and 82%, as presented in Table 2. A coefficient of friction of 0.33 was measured between the surface of the cone tip/sleeve and the material sample.

Table 2. Material data for dry sand of relative density 38% and 82%.

Material property	**38%**	**82%**
E_{50} Young's modulus (kPa)	22,800	38,000
Density (kN/m^3)	16.5	18.2
Poisson's ratio	0.3	0.3
Friction angle (^{o})	32.8	38.3
Dilation angle (^{o})	2.8	8.3
Apparent cohesion (kPa)	0.3	0.3
Pressure coefficient $\boldsymbol{K_0}$	0.41	0.38
Stiffness exponent $\boldsymbol{m_E}$	0.56	0.44

A non-linear variation of the elastic parameters is approximated by setting the Young's modulus as a function of initial minimum principal stress, which is a function of the weight of material above it, K_0 and m_E. Following the work of Brinkgreve *et al.* (2010) the Young's modulus is determined as

$$E = E_{50}\left(\frac{\sigma_v K_0}{p_{ref}}\right)^{m_E}. \qquad (16)$$

The Young's modulus for a MP is set at the start of the analysis and then held constant.

3.2 Validation results

Tip pressure, q_c, against tip penetration depth is presented in *Figure 4* and shows good agreement.

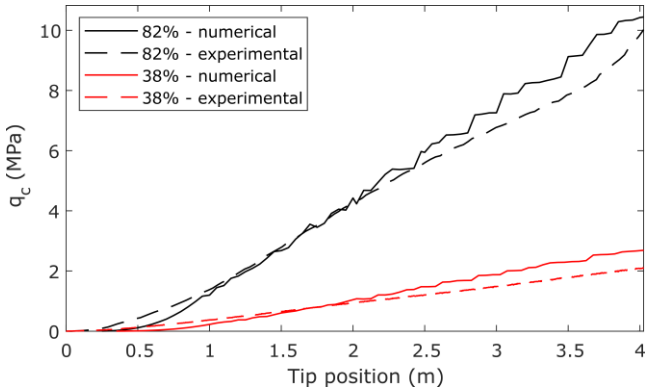

Figure 4. Comparison of numerical CPT against experimental CPT results.

Between 0-0.75 metres the numerical result is more compliant suggesting an underestimation of the initial Young's modulus at the surface, however beyond the initial layer the estimation of the elastic properties and the relatively simple plasticity model are sufficient to achieve accurate results.

There are oscillations in the load-depth curve in *Figure 4*, this is caused by the interaction of the contact occurring at the MP level. An upward oscillation is caused by new MPs coming into contact with the rigid body, whilst a downward oscillation is caused by MPs sliding from the cone tip to the cone sleeve.

3.3 CPT with layered media

The capability of the method to model a layered sand, and the subsequent results, is investigated in this section. The geometry and the grid for the simulations was set up as in *Figure 3* with the sand composed of the two densities from *Table 2.* The sand was distributed such that the first 5 metres at the top of the sample had a different density to the sand below it. Unlike the validation, here the cone penetrates 10 m, and the results are presented in terms of the ratio of the tip position with tip radius, see *Figure 5*, rather than absolute position; the change in sand densities occurs at the ratio 12.4.

The results in *Figure 5* show how the tip pressure varies with relative depth for a range of homogeneous and layered sands. For both the layered sands, the variation of q_c with penetration ratio asymptotes towards the homogeneous result for the deeper sand. This asymptotic behaviour begins earlier than the sand interface at 12.4; this inflection before the interface is also shown experimentally (Xiao, 2023).

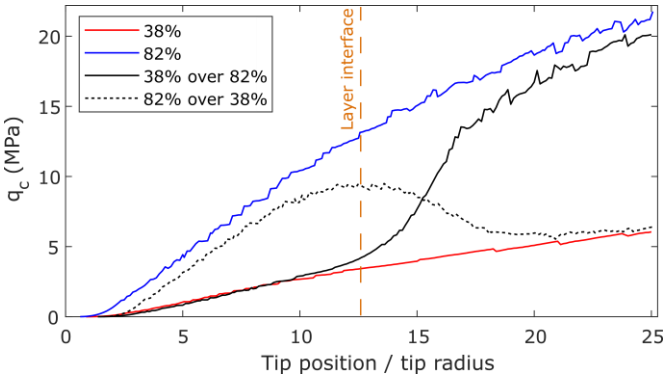

Figure 5. Layered media, the variation of the tip pressure with relative depth for a range of homogeneous and layered sands.

4 CONCLUSION

This paper presents an implicit contact algorithm for the MPM with a rigid body with Coulomb stick-slip friction. The algorithm was validated, and agreed well, with experimental data for homogeneous dry sands ranging in relative density. The algorithm was subsequently applied directly to two-layered sands and provides a useful

tool for the analysis of large deformation geotechnical problems involving soil-structure interaction, not just CPTs.

5 ACKNOWLEDGEMENTS

This work was supported by the Engineering and Physical Sciences Research Council [grant number EP/W000970/1].

6 REFERENCES

Bing, Y., Cortis, M., Charlton, T.J., Coombs, W.M., Augarde, C.E. 2019. B-spline based boundary conditions in the material point method. *Computers & Structures*, **212**, 257-274.

Brinkgreve, R.B.J., Engin, E., & Engin, H. K. 2010. Validation of empirical formulas to derive model parameters for sands. *Numerical methods in geotechnical engineering*, **137**, 142.

Charlton, T.J. 2018. *An implicit Generalised Interpolation Material Point Method for large deformation and gradient elasto-plasticity*, PhD thesis, Durham University, Durham.

Charlton, T.J., Coombs, W.M., Augarde, C.E. 2017. iGIMP: An implicit generalised interpolation material point method for large deformations. *Computers & Structures*, **190**, 108-125.

Coombs, W.M. 2022. Ghost stabilisation of the Material Point Method for stable quasi-static and dynamic analysis of large deformation problems. *arXiv preprint arXiv:2209.10955*.

Coombs, W.M., Augarde, C.E. 2020a. AMPLE: a material point learning environment. *Advances in Engineering Software*, **139**, 102748.

Coombs, W.M., Augarde, C.E., Brennan, A.J., Brown, M.J., Charlton, T.J., Knappett, J.A., Wang, L. 2020b. On Lagrangian mechanics and the implicit material point method for large deformation elasto-plasticity. *Computer Methods in Applied Mechanics and Engineering*, **358**, 112622.

Courant, R., Friedrichs, K., & Lewy, H. 1928. Über die partiellen Differenzengleichungen der mathematischen Physik. *Mathematische annalen*, **100**(1), 32-74.

Cortis, M., Coombs, W.M., Augarde, C.E., Brown, M., Brennan, A., Robinson, S. 2018. Imposition of essential boundary conditions in the material point method. *International Journal for Numerical Methods in Engineering*, **113**(1), 130-152.

Davidson, C., Brown, M., Cerfontaine, B., Knappett, J., Brennan, A., Al-Baghdadi, T., Augarde, C.E., Coombs, W.M., Wang, L., Blake, A., Richards, D., Ball, J.D. 2022. Physical modelling to demonstrate the feasibility of screw piles for offshore jacket supported wind energy structures, *Geotechnique*, **72**(2), 108-126.

Gao, L., Guo, N., Yang, Z.X., Jardine, R.J. 2022. MPM modeling of pile installation in sand: Contact improvement and quantitative analysis. *Computers and Geotechnics*, **151**, 104943.

Guilkey, J., Weiss J. 2003. Implicit time integration for the material point method: Quantitative and algorithmic comparisons with the finite element method. *International Journal for Numerical Methods in Engineering*, **57**, 1323–1338.

Hu, Y., Fang, Y., Ge, Z., Qu, Z., Zhu, Y., Pradhana, A., Jiang, C. 2018. A moving least squares material point method with displacement discontinuity and two-way rigid body coupling. *ACM Transactions on Graphics*, **37**(4), 1-14.

Lei, Z., Wu, B., Wu, S., Nie, Y., Cheng, S., Zhang, C. 2022. A material point-finite element (MPM-FEM) model for simulating three-dimensional soil-structure interactions with the hybrid contact method. *Computers and Geotechnics*, **152**, 105009.

Llano-Serna, M. A., Farias, M. M., Pedroso, D. M. 2016. An assessment of the material point method for modelling large scale run-out processes in landslides. *Landslides*, **13**(5), 1057-1066.

Ma, J., Wang, D., Randolph, M. F. 2014. A new contact algorithm in the material point method for geotechnical simulations. *International Journal for Numerical and Analytical Methods in Geomechanics*, **38**(11), 1197-1210.

Martinelli, M., Vahid, G. 2021. Investigation of the material point method in the simulation of cone penetration tests in dry sand. *Computers and Geotechnics*, **130**, 103923.

Mellett, C. L., Long, D., Carter, G. 2015. Geology of the seabed and shallow subsurface: The Irish Sea.

Moresi, L., Quenette, S., Lemiale, V., Meriaux, C., Appelbe, B., Mühlhaus, H. B. 2007. Computational approaches to studying non-linear dynamics of the crust and mantle. *Physics of the Earth and Planetary Interiors*, **163**(1-4), 69-82.

Nakamura, K., Matsumura, S., Mizutani, T. 2021. Particle-to-surface frictional contact algorithm for material point method using weighted least squares. *Computers and Geotechnics*, **134**, 104069.

Robinson S., Brown M.J., Matsui H., Brennan A., Augarde C.E., Coombs W.M., and Cortis M. 2021. A cone penetration test (CPT) approach to cable plough performance prediction based upon centrifuge model testing, *Canadian. Geotechnical Journal*, **58**(10), 1466-1477.

Roscoe K.H., Burland J.B. 1968. On the generalised stress-strain behaviour of 'wet' clay. In: J Heyman & FA Leckie (eds.), Engineering Plasticity, Cambridge University Press, 535–609.

Sulsky, D., Chen, Z., Schreyer, H.L. 1994. A particle method for history-dependent materials. *Computer Methods in Applied Mechanics and Engineering*, **118**(1-2), 179-196.

Tolooiyan A., Gavin K. 2011. Modelling the cone penetration test in sand using cavity expansion and arbitrary Lagrangian Eulerian finite element methods. *Computers and Geotechnics*, **38**(4), 482-490.

Wang, B., Vardon, P. J., Hicks, M. A. 2016. Investigation of retrogressive and progressive slope failure mechanisms using the material point method. *Computers and Geotechnics*, **78**, 88-98.

Wriggers, P. 2006. *Computational contact mechanics*, Springer, Berlin.

Xiao, L., Lu, L., Wang, Z., He, B., Arai, K. 2023. Estimation of the detection distances of CPT resistance. *Engineering Geology*, **313**, 106953.